Springer Acta Mechanica Sinica

• RESEARCH PAPER •

Acta Mech. Sin., Vol. 39, 323022 (2023)
https://doi.org/10.1007/s10409-023-23022-x

Lagrange's equations for seepage flow in porous media with a mixed Lagrangian-Eulerian description

Li-Xiang Wang[1], Shi-Hai Li[1,2*], and Chun Feng[1,2*]

[1] *Key Laboratory for Mechanics in Fluid Solid Coupling Systems, Institute of Mechanics, Chinese Academy of Sciences, Beijing 100190, China;*
[2] *School of Engineering Science, University of Chinese Academy of Sciences, Beijing 100049, China*

Received April 3, 2023; accepted April 23, 2023; published online August 25, 2023

Most conventional numerical models employ partial differential equations (PDEs) to describe seepage flow problems and use weighted residual and finite difference solution techniques to solve the PDEs. These PDEs are established in view of a spatial point, which mathematically stems from the infinitesimal concept. An alternative approach to such problems is developed. It applies an energy approach, i.e., the Lagrange's equations, to the representation of the seepage flow system, instead of directly resorting to the PDEs. The Lagrange's functional is established on a representative volume element (RVE) by integrating the energy of the RVE. Following a Lagrange formulation, the variation of the functional is conducted with regard to appropriate generalized coordinates. Then the resulting integral equations are considered with the description from the Lagrangian frame into the Eulerian frame for an improved accuracy. Afterwards, the equations are numerically discretized with a cell-centered finite volume method. Finally, two seepage front estimation schemes are presented—one scheme is implemented by local mesh refinement and the other scheme by seepage front movement. The resulting model is a true energy formulation, developed without reference to the partial differential momentum equations. Numerical examples are demonstrated and show that the model generates physically sound results.

Lagrange's equations, Lagrangian-Eulerian model, Seepage flow in porous media, Cell-centered finite volume method, Seepage front

---

Citation: L.-X. Wang, S.-H. Li, and C. Feng, Lagrange's equations for seepage flow in porous media with a mixed Lagrangian-Eulerian description, Acta Mech. Sin. **39**, 323022 (2023), https://doi.org/10.1007/s10409-023-23022-x

1. Introduction

Darcy's law fundamentally describes the phenomenon of a fluid flowing through a porous medium. It was initially established by Henry Darcy in 1856 based on the results of experiments on the flow of water through beds of sand [1]:

$$Q = kA\frac{(h_1 - h_2)}{L}, \tag{1}$$

where Q is the volumetric discharge; k is the hydraulic conductivity; A stands for the seepage area; L stands for the seepage length; h_1 and h_2 are water potentials. In 1986, Whitaker [2] analyzed Stokes flow problems using the method of volume averaging and derived spatial deviations of pressure and velocity in Stokes equations, theoretically leading to Darcy's law.

Darcy's law plays a critical role in various engineering scenarios. In hydrogeology, it is to flow water through a permeable aquifer [3]. In petroleum engineering, it is to describe oil, gas, and water flows through reservoirs [4]. In hydraulic engineering, it is to analyze dam stability under seepage flow conditions [5]. In underground storage engineering, it is to prevent oil leakage from water-sealed caverns [6]. In ocean engineering, it is to control seawater intrusion in coastal aquifers [7]. In mining engineering, it is to understand the mechanism of coal-gas outbursts [8]. More applications can be found in the editorial review paper [9].

---

*Corresponding authors. E-mail addresses: shli@imech.ac.cn (Shi-Hai Li); fengchun@imech.ac.cn (Chun Feng)
Executive Editor: Xueming Shao

Darcy's law indicates that fluid flow in porous media behaves linearly. In fact, non-linear flow behaviors also exist in porous media, as indicated by Majid Hassanizadeh and Leijnse [10], Liu and Masliyah [11], Zhou et al. [12], and Tao et al. [13]. Especially in the process of hydraulic fracturing of low-permeability shales, non-linear flows cannot be ignored [14]. Therefore, non-linear seepage laws such as Forchheimer equation [15] were established to describe such phenomena. Darcy's law or other non-linear law with the conservation of mass equation forms the basic partial differential equations (PDEs) for seepage problems.

Conventional numerical models employ the PDEs to describe seepage flows and use weighted residual and finite difference solution techniques to solve the seepage problems. For example, at early days, Zienkiewicz et al. [16] applied finite element method (FEM) to steady-state seepage analysis; Jeppson [17] employed finite difference method (FDM) to solve free-surface flow through nonhomogeneous porous media; Neuman and Witherspoon [18] used FEM to analyze steady seepage problems with a free surface; Neuman [19] developed a Galerkin-type FEM to solve transient seepage problems in saturated-unsaturated porous media. More recently, Das et al. [20] compared different FDM algorithms used in numerical simulation of two-dimensional single-phase saturated porous media flows; Zheng et al. [21] presented a variational inequality formulation in FEM for seepage problems with free surfaces; Chávez-Negrete et al. [22] proposed a generalized FDM to solve the Richards' equation; Sharma et al. [23] developed a moving-mesh type FEM for the computation of transient unconfined seepage flow through porous media. Moreover, some novel numerical methods have been developed for seepage flow analysis, such as finite volume method (FVM) [24-26], numerical manifold method (NMM) [27-30], meshfree method [31, 32], FE-meshfree method [33], virtual element method (VEM) [34] and so forth. The abbreviations are listed in Appendix A.

The above numerical models are established on the basis of PDEs, by means of spatial point description of physical laws. An alternative energy approach, i.e., the Lagrange or Hamilton equation approach [35, 36], is presented in this paper to the representation of a seepage flow system, instead of directly resorting to the PDEs. The Lagrange or Hamilton equation approach has been successfully applied to many fields, such as viscous compressible fluid dynamics [37, 38], impact dynamics with perforation and fragmentation [39], thermofluid dynamics [40], reacting thermofluid dynamics [41], and so forth. As for continuum mechanics problems, Liang et al. [42] recently gave an excellent review on the applications of the Lagrange-Hamilton approach to such problems. Nonetheless, to our best knowledge, the application of this approach to seepage flow problems has been seldom reported.

In this paper, we present a novel numerical model for transient seepage flow analysis based on the Lagrange equation approach [35, 36]. The model is established on a representative volume element (RVE) instead of being differentially described at a spatial point. The variation of the Lagrangian on the RVE results in a set of integral equations for the seepage flow system. Then the equations are formulated from the Lagrangian frame into the Eulerian frame for an improved accuracy. Afterwards, the equations are numerically discretized with a cell-centered finite volume method (CCFVM) [43, 44]. Finally, two seepage front estimation schemes are introduced into the model for a better flux approximation. The model is termed the Lagrangian-Eulerian (LE) model due to its mixed LE description nature.

The presented LE model is a true energy formulation, developed without reference to partial differential momentum equations. The LE model is capable of dealing with both linear and non-linear flows provided a suitable seepage law is introduced into the Lagrangian. The LE model obtains more accurate pressure gradients, flow rates and fluxes since it considers seepage front estimation. Thus, the fluid leak-off in hydraulic fracturing can be simulated more accurately, compared with the conventional numerical models, which directly resort to the discretization of the PDEs.

The paper is organized as follows. In Sect. 2, we elaborate the establishment of the Lagrangian of a seepage flow system and the variation of the Lagrangian through the canonical Lagrange's equations. In Sect. 3, we transform the integrated seepage equations from the Lagrangian frame into the Eulerian frame. After transformation, a CCFVM is used to discretize the mixed Lagrangian-Eulerian seepage equations in Sect. 4. In Sect. 5, two seepage front estimation schemes are introduced—the LER scheme and the LEM scheme. Afterwards, two examples in Sects. 6 and 7 are demonstrated to show the advantages of the proposed LE model. Finally, conclusions are drawn in Sect. 8 regarding the proposed LE model.

2. Lagrange's equations for seepage flow system

2.1 Geometric representation of the RVE

A porous medium consists of two phases—one is the solid matrix and the other is the fluid in pores, as illustrated in

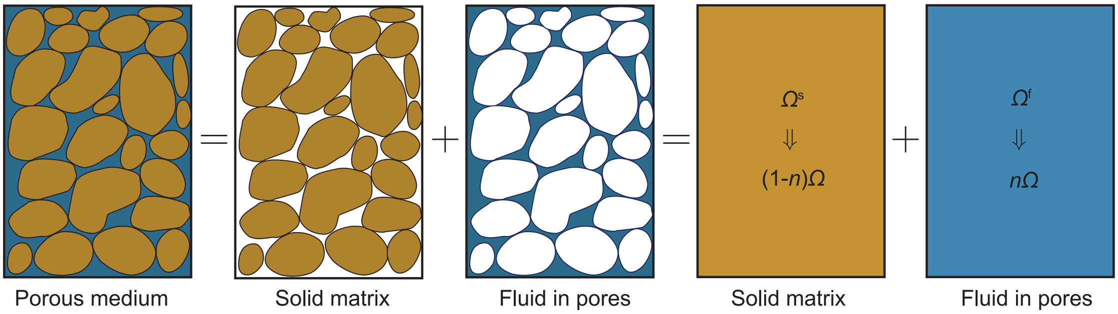

Figure 1 Geometric representation of the RVE for a porous medium.

Fig. 1. Both phases can be viewed as a continuous medium and their percentages are n and $(1-n)$, respectively. The percentage of the fluid phase n is also termed porosity. The space that the solid phase occupies is denoted as Ω^{s} whereas the space that the fluid phase occupies is denoted as Ω^{f}. The total space of the porous medium is denoted as Ω. From a mixture point of view [45], we can assume that the following constituent equations hold

$$\begin{cases} \Omega = \Omega^{\mathrm{s}} + \Omega^{\mathrm{f}}, \\ \Omega^{\mathrm{s}} = (1-n)\Omega, \\ \Omega^{\mathrm{f}} = n\Omega. \end{cases} \tag{2}$$

Under the assumption of Eq. (2), the energy integration on Ω^{s} or Ω^{f} can be transformed into the energy integration on Ω.

2.2 Lagrange's energy functional (Lagrangian)

The energy of solid matrix in a porous medium consists of the following terms:

(1) Kinetic energy of solid matrix;
(2) Strain energy of solid matrix;
(3) Work done by fluid pressure on solid matrix;
(4) Work done by body force on solid matrix;
(5) Work done by traction force on solid matrix.

Thus, the integral form of the Lagrange's energy functional for solid matrix (Lagrangian of the solid phase) L_{s} can be expressed as

$$\begin{aligned} L_{\mathrm{s}} = & \int_{\Omega} \frac{1}{2}(1-n)\rho_{\mathrm{s}}\mathbf{v}_{\mathrm{s}}^2\,\mathrm{d}V - \int_{\Omega} \frac{1}{2}\boldsymbol{\sigma}_{\mathrm{s}} : \boldsymbol{\varepsilon}_{\mathrm{s}}\,\mathrm{d}V \\ & + \int_{\Omega} \frac{1}{2}(1-n)p_{\mathrm{f}}\mathbf{i} : \boldsymbol{\varepsilon}_{\mathrm{s}}\,\mathrm{d}V \\ & + \int_{\Omega} (1-n)\rho_{\mathrm{s}}\mathbf{g}\cdot\mathbf{u}_{\mathrm{s}}\,\mathrm{d}V + \int_{\partial\Omega} \mathbf{u}_{\mathrm{s}}\cdot\bar{\boldsymbol{\sigma}}_{\mathrm{s}}\cdot\mathbf{n}\,\mathrm{d}S, \end{aligned} \tag{3}$$

where the first term is the kinetic energy of solid matrix in terms of solid density ρ_{s} and solid velocity $\mathbf{v}_{\mathrm{s}}$; the second term is the strain energy of solid matrix in terms of solid stress tensor $\boldsymbol{\sigma}_{\mathrm{s}}$ and solid strain tensor $\boldsymbol{\varepsilon}_{\mathrm{s}}$; the third term is the work done by fluid pressure p_{f} on solid matrix with $\mathbf{i}$ the third-order identity tensor; the fourth term is the work done by body force $\mathbf{b}_{\mathrm{s}} = \rho_{\mathrm{s}}\mathbf{g}$ along displacement $\mathbf{u}_{\mathrm{s}}$, with $\mathbf{g}$ the gravitational acceleration; and the last term is the work done by traction force $\bar{\boldsymbol{\sigma}}_{\mathrm{s}}$ on the solid boundary $\partial\Omega$ with a unit outer normal vector $\mathbf{n}$.

The energy of fluid in pores in a porous medium consists of the following terms:

(1) Kinetic energy of fluid in pores;
(2) Strain energy of fluid in pores;
(3) Work done by body force on fluid in pores;
(4) Work done by boundary pressure on fluid in pores.

Thus, the integral form of the Lagrange's energy functional for fluid in pores (Lagrangian of the fluid phase) L_{f} can be expressed as

$$\begin{aligned} L_{\mathrm{f}} = & \int_{\Omega} \frac{1}{2}n\rho_{\mathrm{f}}\mathbf{v}_{\mathrm{f}}^2\,\mathrm{d}V + \int_{\Omega} \frac{1}{2}np_{\mathrm{f}}\mathbf{i} : \boldsymbol{\varepsilon}_{\mathrm{f}}\,\mathrm{d}V \\ & + \int_{\Omega} n\rho_{\mathrm{f}}\mathbf{g}\cdot\mathbf{u}_{\mathrm{f}}\,\mathrm{d}V - \int_{\partial\Omega} \mathbf{u}_{\mathrm{f}}\cdot(np_{\mathrm{f}}\mathbf{i})\cdot\mathbf{n}\,\mathrm{d}S, \end{aligned} \tag{4}$$

where the first term is the kinetic energy of fluid in pores in terms of fluid density ρ_{f} and fluid velocity $\mathbf{v}_{\mathrm{f}}$; the second term is the strain energy of fluid in pores in terms of fluid pressure p_{f} and the spatial derivatives of fluid displacements $\boldsymbol{\varepsilon}_{\mathrm{f}}$; the third term is the work done by body force $\mathbf{b}_{\mathrm{f}} = \rho_{\mathrm{f}}\mathbf{g}$ on fluid in pores along displacement $\mathbf{u}_{\mathrm{f}}$; and the last term is the work done by boundary pressure on fluid in pores.

Besides, the right-hand side (RHS) in Lagrange's equations should be specified. The RHS of solid matrix and the RHS of fluid in pores in Lagrange's equations can be respectively written as

$$\mathbf{f}_{\mathrm{s}} = \int_{\Omega} \frac{n^2\rho_{\mathrm{f}}g}{k}(\mathbf{v}_{\mathrm{f}} - \mathbf{v}_{\mathrm{s}})\,\mathrm{d}V - \int_{\Omega} p_{\mathrm{f}}\nabla n\,\mathrm{d}V, \tag{5}$$

$$\mathbf{f}_{\mathrm{f}} = -\mathbf{f}_{\mathrm{s}} = -\int_{\Omega} \frac{n^2\rho_{\mathrm{f}}g}{k}(\mathbf{v}_{\mathrm{f}} - \mathbf{v}_{\mathrm{s}})\,\mathrm{d}V + \int_{\Omega} p_{\mathrm{f}}\nabla n\,\mathrm{d}V, \tag{6}$$

where g is the value of the gravitational acceleration and k is the hydraulic conductivity. The non-conservative forces in Eqs. (5) and (6) are the frictional forces between fluid and solid, and the buoyancy term is caused by porosity gradients [46].

2.3 Canonical Lagrange's equations

The canonical Lagrange's equation reads [36]

$$\frac{\mathrm{d}}{\mathrm{d}t}\frac{\partial L}{\partial \dot{q}} - \frac{\partial L}{\partial q} - f = 0, \tag{7}$$

where L is the well-known Lagrangian (i.e., the Lagrange's energy functional); q is the generalized coordinate; $\dot{q}$ is the temporal derivative of the generalized coordinate; f is the generalized non-conservative force.

Here we take $\mathbf{u}_\mathrm{s}$ as the generalized coordinates for solid matrix. Therefore, the canonical Lagrange's equations for solid matrix can be written as

$$\frac{\mathrm{d}}{\mathrm{d}t}\frac{\partial L_\mathrm{s}}{\partial \mathbf{v}_\mathrm{s}} - \frac{\partial L_\mathrm{s}}{\partial \mathbf{u}_\mathrm{s}} - \mathbf{f}_\mathrm{s} = \mathbf{0}. \tag{8}$$

By inserting Eqs. (3) and (5) into the canonical Lagrange's equation (8), we can obtain the integral form of the governing equations for solid deformation under generalized coordinate system:

$$\begin{aligned}&\frac{\mathrm{d}}{\mathrm{d}t}\int\limits_{\Omega}(1-n)\rho_\mathrm{s}\mathbf{v}_\mathrm{s}\,\mathrm{d}V - \int\limits_{\Omega}\nabla\cdot\boldsymbol{\sigma}_\mathrm{s}\,\mathrm{d}V\\ &+\int\limits_{\Omega}(1-n)\nabla p_\mathrm{f}\,\mathrm{d}V - \int\limits_{\Omega}(1-n)\rho_\mathrm{s}\mathbf{g}\,\mathrm{d}V\\ &-\int\limits_{\Omega}\frac{n^2\rho_\mathrm{f}g}{k}(\mathbf{v}_\mathrm{f}-\mathbf{v}_\mathrm{s})\,\mathrm{d}V = \mathbf{0}.\end{aligned} \tag{9}$$

Then we take $\mathbf{u}_\mathrm{f}$ as the generalized coordinates for fluid in pores. Thus the canonical Lagrange's equations for fluid in pores can be written as

$$\frac{\mathrm{d}}{\mathrm{d}t}\frac{\partial L_\mathrm{f}}{\partial \mathbf{v}_\mathrm{f}} - \frac{\partial L_\mathrm{f}}{\partial \mathbf{u}_\mathrm{f}} - \mathbf{f}_\mathrm{f} = \mathbf{0}. \tag{10}$$

By inserting Eqs. (4) and (6) into the canonical Lagrange's equation (10), we can obtain the integral form of the governing equations for seepage flow under generalized coordinate system

$$\begin{aligned}&\frac{\mathrm{d}}{\mathrm{d}t}\int\limits_{\Omega}n\rho_\mathrm{f}\mathbf{v}_\mathrm{f}\,\mathrm{d}V + \int\limits_{\Omega}n\nabla p_\mathrm{f}\,\mathrm{d}V - \int\limits_{\Omega}n\rho_\mathrm{f}\mathbf{g}\,\mathrm{d}V\\ &+\int\limits_{\Omega}\frac{n^2\rho_\mathrm{f}g}{k}(\mathbf{v}_\mathrm{f}-\mathbf{v}_\mathrm{s})\,\mathrm{d}V = \mathbf{0}.\end{aligned} \tag{11}$$

Equation (11) is the seepage flow equations derived from the canonical Lagrange's equations. Note that it is formulated in a Lagrangian frame. By contrast, the conventional governing equations for seepage flow, i.e., the Darcy's law, read

$$\begin{aligned}\mathbf{V} &= -\frac{k}{\rho_\mathrm{f}g}(\nabla p_\mathrm{f} - \rho_\mathrm{f}\mathbf{g})\\ &= -\frac{K}{\mu}(\nabla p_\mathrm{f} - \rho_\mathrm{f}\mathbf{g})\\ &= -\kappa(\nabla p_\mathrm{f} - \rho_\mathrm{f}\mathbf{g}),\end{aligned} \tag{12}$$

where K is the permeability, μ is the dynamic viscosity, and κ is the permeability coefficient. Note that different parameter systems $[(k, \rho_\mathrm{f}, g)$ or (K, μ) or $\kappa]$ are preferred in different fields. We present the detailed comparisons among different parameter systems of seepage flow in Appendix B.

By comparing Eqs. (11) and (12), we can learn that the seepage flow equation (11) derived from the canonical Lagrange's equation is in an integral form and that it considers the inertial term $\frac{\mathrm{d}}{\mathrm{d}t}\int_\Omega n\rho_\mathrm{f}\mathbf{v}_\mathrm{f}\,\mathrm{d}V$. Darcy's law is generally valid when the flow is laminar, i.e., the Reynolds' number $Re \leq 1$ [47]. This implies a small seepage velocity, and thus the inertia term has been neglected. If we ignore this term in Eq. (11) and denote the seepage velocity as

$$\mathbf{V} = n(\mathbf{v}_\mathrm{f} - \mathbf{v}_\mathrm{s}), \tag{13}$$

Eq. (11) can degenerate into Eq. (12).

Remark 1. In the Lagrangian-Eulerian model to be presented, the fluid velocity at the seepage front may be large (see Sect. 5.1). Thus, the Reynolds' number $Re \equiv \rho_\mathrm{f}v_\mathrm{f}d/\mu$ could exceed 1. In this case, the large seepage velocity may cause significant inertia effect.

3. Mixed Lagrangian-Eulerian description

Assume that the solid velocity $\mathbf{v}_\mathrm{s}$ is very small, so this term in Eq. (11) can be neglected. No longer considering the solid effect, we can omit for simplicity in the remainder of this paper all the subscripts "f" in the fluid equations. Consider the integration of the inertial term in Eq. (11) on a RVE Ω as illustrated in Fig. 2. We also assume that the porosity n changes little. Therefore, we just consider the derivative of $\rho\mathbf{v}$ from time $(t-\Delta t)$ to time t. Based on the variable limit integral formula, the derivative of the integration can be transformed into:

$$\frac{\mathrm{d}}{\mathrm{d}t}\int\limits_{\Omega}\rho\mathbf{v}\,\mathrm{d}V = \int\limits_{\Omega}\frac{\mathrm{d}}{\mathrm{d}t}(\rho\mathbf{v})\,\mathrm{d}V + \frac{\mathrm{d}}{\mathrm{d}t}\int\limits_{\Delta\Omega}\rho\mathbf{v}\,\mathrm{d}V, \tag{14}$$

where Ω and $\Delta\Omega$ are shown in Fig. 2 and they can be expressed as

$$\Omega = \Omega_1 + \Omega_2, \quad \Delta\Omega = \Omega_3 - \Omega_1. \tag{15}$$

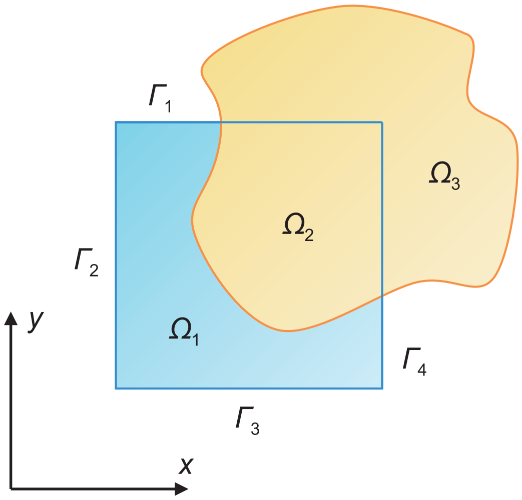

Figure 2 Volume change of a RVE after time increment Δt.

Equation (14) shows that the rate of change in momentum consists of the local rate of change in momentum and the boundary rate of change in momentum. The boundary rate of change in momentum in two dimensions can be written as

$$\begin{aligned}\frac{\mathrm{d}}{\mathrm{d}t}\int_{\Delta\Omega}\rho\mathbf{v}\,\mathrm{d}V =&\frac{\mathrm{d}}{\mathrm{d}t}\int_{x_0}^{x_1}\mathrm{d}x\int_{y_1^d=x_1^d(x,t)}^{y_1^u=x_1^u(x,t)}\rho\mathbf{v}\,\mathrm{d}y\\ &+\frac{\mathrm{d}}{\mathrm{d}t}\int_{x_0}^{x_1}\mathrm{d}x\int_{y_2^d=x_2^d(x,t)}^{y_2^u=x_2^u(x,t)}\rho\mathbf{v}\,\mathrm{d}y\\ &+\frac{\mathrm{d}}{\mathrm{d}t}\int_{y_0}^{y_1}\mathrm{d}y\int_{x_1^d=y_1^d(x,t)}^{x_1^u=y_1^u(y,t)}\rho\mathbf{v}\,\mathrm{d}x\\ &+\frac{\mathrm{d}}{\mathrm{d}t}\int_{y_0}^{y_1}\mathrm{d}y\int_{x_2^d=y_2^d(y,t)}^{x_2^u=y_2^u(y,t)}\rho\mathbf{v}\,\mathrm{d}x,\end{aligned}\tag{16}$$

where the limits on the integration stands for the edges Γ_i in Fig. 2, which can be expressed in details as

$$\begin{cases}\Gamma_1=[x_0,x_1]\times[y_1^d,y_1^u],\\ \Gamma_2=[y_0,y_1]\times[x_1^d,x_1^u],\\ \Gamma_3=[x_0,x_1]\times[y_2^d,y_2^u],\\ \Gamma_4=[y_0,y_1]\times[x_2^d,x_2^u].\end{cases}\tag{17}$$

Without loss of generality, consider the first term in Eq. (16). According to the integral mean value theorem, we have

$$\begin{aligned}&\frac{\mathrm{d}}{\mathrm{d}t}\int_{x_0}^{x_1}\mathrm{d}x\int_{x_1^d(x,t)}^{x_1^u(x,t)}\rho\mathbf{v}\mathrm{d}y=\int_{x_0}^{x_1}\left(\frac{\mathrm{d}}{\mathrm{d}t}\int_{x_1^d(x,t)}^{x_1^u(x,t)}\rho\mathbf{v}\mathrm{d}y\right)\mathrm{d}x\\ &\approx\int_{x_0}^{x_1}\rho\mathbf{v}\Big|_{y=\frac{x_1^u+x_1^d}{2}}\frac{\mathrm{d}}{\mathrm{d}t}\left(x_1^u-x_1^d\right)\mathrm{d}x,\end{aligned}\tag{18}$$

where $\frac{\mathrm{d}}{\mathrm{d}t}(x_1^u-x_1^d)$ denotes the rate of change of displacement on the boundary. Consider the time period from $(t-\Delta t)$ to t, and this term can be written as

$$\frac{\mathrm{d}}{\mathrm{d}t}\left(x_1^u-x_1^d\right)=v^t-v^{t-\Delta t}.\tag{19}$$

Similarly, we can get a general formula expressed in the form of a vector, which can be written as

$$\frac{\mathrm{d}}{\mathrm{d}t}\int_{\Delta\Omega}\rho\mathbf{v}\,\mathrm{d}V=\int_{\partial\Omega(t)}\rho\mathbf{v}\left[\left(\mathbf{v}^t-\mathbf{v}^{t-\Delta t}\right)\cdot\mathbf{n}\right]\mathrm{d}S.\tag{20}$$

By inserting Eq. (20) into Eq. (11) and ignoring the velocity of solid, we obtain

$$\begin{aligned}&\int_{\Omega}\frac{\mathrm{d}}{\mathrm{d}t}(n\rho\mathbf{v})\,\mathrm{d}V+\int_{\Omega}n\nabla p\,\mathrm{d}V-\int_{\Omega}n\rho\mathbf{g}\,\mathrm{d}V\\ &+\int_{\Omega}\frac{n^2\rho g}{k}\mathbf{v}\,\mathrm{d}V=\int_{\partial\Omega(t)}\rho\mathbf{v}(\Delta\mathbf{v}^t\cdot\mathbf{n})\,\mathrm{d}S,\end{aligned}\tag{21}$$

where we denote $\Delta\mathbf{v}^t=\mathbf{v}^t-\mathbf{v}^{t-\Delta t}$ for simplicity.

Equation (21) is the so-called integrated seepage equations in a mixed Lagrangian-Eulerian frame or the LE model. It is different from the seepage equation in a fully Lagrangian frame:

$$\frac{\mathrm{d}}{\mathrm{d}t}(n\rho\mathbf{v})+n\nabla p-n\rho\mathbf{g}+\frac{n^2\rho g}{k}\mathbf{v}=\mathbf{0}.\tag{22}$$

Equation (22) does not consider the surface integration term $\int_{\partial\Omega(t)}\rho\mathbf{v}(\Delta\mathbf{v}^t\cdot\mathbf{n})\,\mathrm{d}S$ on a varying boundary $\partial\Omega(t)$ caused by numerical discretization on a representative volume element. This term may play an important role in stabilization of non-linear effects.

4. Discretization with cell-centered FVM

4.1 Distribution of velocity and pressure variables

As illustrated in Fig. 3, the nodal distribution of velocity and pressure shows that the pressure variables lie in the center of a cell and the velocity variables lie in the center of a face (in 3D) or the mid-point of an edge (in 2D). The solid and hollow boxes are both pressure variables, and the solid and hollow circles are both velocity variables. The solid boxes stand for the inner pressure variables and the hollow boxes stand for the boundary pressure variables. The solid circles are inner velocity variables and the hollow circles are boundary velocity variables.

4.2 Cell-centered finite volume method

By using the Euler's forward scheme, Eq. (21) can be discretized in the temporal domain as

$$\int_{\Omega}\left(n\rho\frac{\Delta\mathbf{v}^t}{\Delta t}+n\nabla p^{t+\Delta t}-n\rho\mathbf{g}+\frac{n^2\rho g}{k}\mathbf{v}^{t+\Delta t}\right)\mathrm{d}V$$

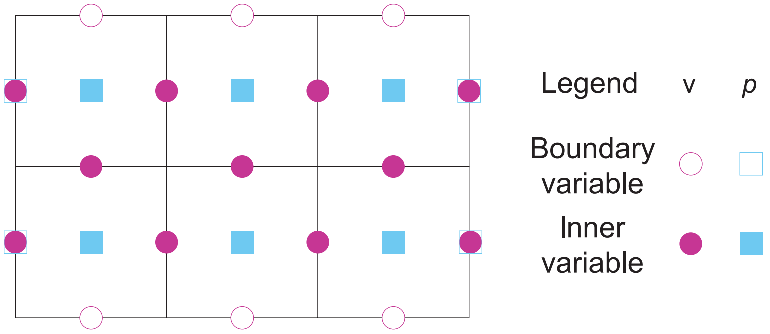

Figure 3 Distribution of velocity ($\mathbf{v}$) and pressure (p) variables in cell-centered finite volumes.

$$= \int_{\partial\Omega(t)} \rho \mathbf{v}^t (\Delta \mathbf{v}^t \cdot \mathbf{n})\, \mathrm{d}S. \tag{23}$$

Taking a finite volume cell as the integration volume, Eq. (23) can be numerically discretized in the spatial domain as

$$\left(n\rho \frac{\Delta \mathbf{v}^t}{\Delta t} + n\nabla p^{t+\Delta t} - n\rho \mathbf{g} + \frac{n^2 \rho g}{k} \mathbf{v}^{t+\Delta t}\right) V_{\mathrm{C}} = \sum_{\mathrm{F}} \rho \mathbf{v}_{\mathrm{F}}^t \left(\Delta \mathbf{v}_{\mathrm{F}}^t \cdot \mathbf{n}_{\mathrm{F}} S_{\mathrm{F}}\right), \tag{24}$$

where V_{C} is the volume of the cell, F denotes the face of the cell and $\Delta \mathbf{v}_{\mathrm{F}}^t$ stands for the velocity difference between the last two time steps on face F.

From Eq. (24), we can obtain

$$\mathbf{v}^{t+\Delta t} = -\frac{k}{ng}\left(\frac{\nabla p^{t+\Delta t}}{\rho} - \mathbf{g}\right) - \frac{k}{ng}\left(\frac{\Delta \mathbf{v}^t}{\Delta t}\right) - \frac{k}{ng} \sum_{\mathrm{F}} \left[\mathbf{v}_{\mathrm{F}}^t \left(\Delta \mathbf{v}_{\mathrm{F}}^t \cdot \mathbf{n}_{\mathrm{F}}\right) \frac{S_{\mathrm{F}}}{V_{\mathrm{C}}}\right]. \tag{25}$$

For any common face F of two adjacent finite volume cells Ω_i and Ω_j, the face velocity can be expressed as

$$\mathbf{v}_{\mathrm{F}}^{t+\Delta t} = -\frac{k}{ng}\left(\frac{\nabla p_{\mathrm{C}}^{t+\Delta t}}{\rho} - \mathbf{g}\right) - \frac{k}{ng}\left(\frac{\Delta \mathbf{v}_{\mathrm{F}}^t}{\Delta t}\right) - \frac{k}{ng} \sum_{\mathrm{F}} \left[\mathbf{v}_{\mathrm{F}}^t \left(\Delta \mathbf{v}_{\mathrm{F}}^t \cdot \mathbf{n}_{\mathrm{F}}\right) \frac{S_{\mathrm{F}}}{V_{\mathrm{C}}}\right], \tag{26}$$

where ∇p_{C} denotes the pressure gradient across the two adjacent cells.

If we denote the LE seepage velocity as $\mathbf{V}_{\mathrm{F}}^{t+\Delta t} = n\mathbf{v}_{\mathrm{F}}^{t+\Delta t}$, Eq. (26) can be formulated into

$$\mathbf{V}_{\mathrm{F}}^{t+\Delta t} = \underbrace{-\frac{k}{g}\left(\frac{\nabla p_{\mathrm{C}}^{t+\Delta t}}{\rho} - \mathbf{g}\right)}_{\mathbf{V}_1} \underbrace{-\frac{k}{g}\left(\frac{\Delta \mathbf{v}_{\mathrm{F}}^t}{\Delta t}\right)}_{\mathbf{V}_2} \underbrace{-\frac{k}{g} \sum_{\mathrm{F}} \left[\mathbf{v}_{\mathrm{F}}^t \left(\Delta \mathbf{v}_{\mathrm{F}}^t \cdot \mathbf{n}_{\mathrm{F}}\right) \frac{S_{\mathrm{F}}}{V_{\mathrm{C}}}\right]}_{\mathbf{V}_3}. \tag{27}$$

The velocity in Eq. (27) consists of three terms: $\mathbf{V}_1$, $\mathbf{V}_2$, and $\mathbf{V}_3$, which denote the Darcy's seepage velocity, the inertia seepage velocity and the discretization velocity, respectively.

The fluid conservation equation for seepage flow can be written as

$$\frac{n}{K_{\mathrm{f}}} \frac{\mathrm{d}p}{\mathrm{d}t} + \nabla \cdot \mathbf{V} = 0, \tag{28}$$

where K_{f} is bulk modulus of the fluid.

Discretizing the above equation (28) on the temporal domain with the Euler's forward scheme, we obtain

$$p^{t+\Delta t} - p^t = -\frac{K_{\mathrm{f}}}{n}\left(\nabla \cdot \mathbf{V}^t\right) \Delta t. \tag{29}$$

Integrating Eq. (29) over a cell Ω_i, we get

$$\int_{\Omega_i} \left(p^{t+\Delta t} - p^t\right) \mathrm{d}V = -\frac{K_{\mathrm{f}} \Delta t}{n} \int_{\Omega_i} \left(\nabla \cdot \mathbf{V}^t\right) \mathrm{d}V. \tag{30}$$

According to the Gauss divergence theorem, the volume integration on the RHS can be transformed into a surface integration:

$$\int_{\Omega_i} \left(\nabla \cdot \mathbf{V}^t\right) \mathrm{d}V = \oint_{\partial\Omega_i} (\mathbf{V}^t \cdot \mathbf{n})\, \mathrm{d}S = \oint_{\partial\Omega_i} (\mathbf{V}_1^t \cdot \mathbf{n} + \mathbf{V}_2^t \cdot \mathbf{n} + \mathbf{V}_3^t \cdot \mathbf{n})\, \mathrm{d}S. \tag{31}$$

Based on the cell-centered FVM [43, 44], the first term on the RHS of Eq. (31) can be formulated as

$$q_{i,1}^t = \oint_{\partial\Omega_i} (\mathbf{V}_1^t \cdot \mathbf{n})\, \mathrm{d}S = \sum_j T_{ij}(p_i^t - p_j^t), \tag{32}$$

where $q_{i,1}^t$ is the inflow rate of cell Ω_i from adjacent cells (Ω_j) and T_{ij} is the transmissibility between the adjacent cells Ω_i and Ω_j. The formulation of Eq. (32) is detailed in Appendix C.

The second and third terms on the RHS of Eq. (31) can be respectively given by

$$q_{i,2}^t = \oint_{\partial\Omega_i} (\mathbf{V}_2^t \cdot \mathbf{n})\, \mathrm{d}S = \sum_{\mathrm{F}_i} \left(\mathbf{V}_{2,\mathrm{F}_i}^t \cdot \mathbf{n}_{\mathrm{F}_i} S_{\mathrm{F}_i}\right), \tag{33}$$

$$q^t_{i,3} = \oint_{\partial\Omega_i} (\mathbf{V}^t_3 \cdot \mathbf{n})\, \mathrm{d}S = \sum_{\mathrm{F}_i} \left(\mathbf{V}^t_{3,\mathrm{F}_i} \cdot \mathbf{n}_{\mathrm{F}_i} S_{\mathrm{F}_i}\right), \tag{34}$$

where F_i stands for the face of cell Ω_i.

Plugging Eqs. (32)-(34) into Eq. (30), we can obtain the pressure update

$$p_i^{t+\Delta t} - p_i^t = -\frac{K_\mathrm{f}\Delta t}{nV_i}\left(q^t_{i,1} + q^t_{i,2} + q^t_{i,3}\right), \tag{35}$$

where V_i denotes the volume of Ω_i.

4.3 Stability condition

It should be mentioned that the explicit time integration scheme restricts the time step Δt below a critical value Δt_crit to meet the stability condition [48, 49]:

$$r = \frac{\alpha\Delta t}{h^2_\mathrm{min}} < \frac{1}{2}, \tag{36}$$

where r is the stability ratio; h_min is the minimum mesh size; α is a composite parameter similar to the diffusion coefficient:

$$\alpha = \frac{KK_\mathrm{f}}{\mu n}. \tag{37}$$

Thus, we can obtain from Eqs. (36) and (37) the admissible time step:

$$\Delta t < \Delta t_\mathrm{crit} = \frac{h^2_\mathrm{min}}{2\alpha} = \frac{\mu n h^2_\mathrm{min}}{2KK_\mathrm{f}}. \tag{38}$$

5. Seepage front estimation

5.1 Estimation equations

In conventional seepage flow (CSF) model, the seepage front is assumed to reach the element boundary $x = L$ immediately, as shown in Fig. 4. Under this assumption, the seepage velocity and fluid flux can be respectively calculated as

$$v_\mathrm{CSF} = -\frac{K}{\mu}\frac{\partial P}{\partial x} = \frac{K}{\mu}\frac{\Delta P}{L/2}, \tag{39}$$

$$Q_\mathrm{CSF} = A \cdot v_\mathrm{CSF} \cdot \Delta t, \tag{40}$$

where ΔP is the pressure difference; A is the flow area; Δt is the flow duration. Here we can take the flow duration as the time step, which can be estimated by Eq. (38).

The computed pressure gradient in Eq. (39) is smaller than the real one and hence the computed fluid flux is not physically reliable. To tackle this issue, we propose the LE model, which dynamically estimates the seepage front for a better accuracy.

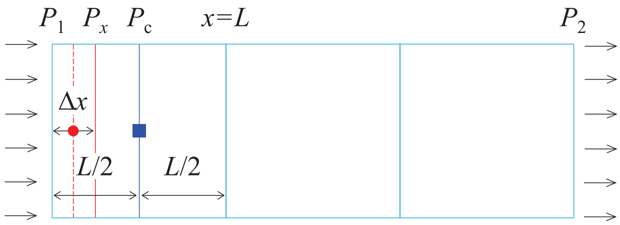

Figure 4 Estimation for seepage front.

Instead of presetting the location of the seepage front, the LE model estimates the seepage front at an unknown coordinate Δx, as shown in Fig. 4. In this way, the pressure gradients $\Delta P = P_1 - P_x$ can be captured more accurately. Thus, the seepage velocity can be obtained from a more reliable pressure gradient:

$$v_\mathrm{LE} = -\frac{K}{\mu}\frac{\partial P}{\partial x} = \frac{K}{\mu}\frac{\Delta P}{\Delta x/2} = \frac{K}{\mu}\frac{\Delta P}{(v_\mathrm{LE} \cdot \Delta t)/2}. \tag{41}$$

Solving Eq. (41) gives the seepage velocity:

$$v_\mathrm{LE} = \sqrt{\frac{2K}{\mu}\frac{\Delta P}{\Delta t}}. \tag{42}$$

Based on Eq. (42), the seepage front Δx and the fluid flux Q_LE can be respectively obtained:

$$\Delta x = v_\mathrm{LE} \cdot \Delta t = \sqrt{\frac{2K \cdot \Delta P \cdot \Delta t}{\mu}}, \tag{43}$$

$$Q_\mathrm{LE} = A \cdot \Delta x = A\sqrt{\frac{2K \cdot \Delta P \cdot \Delta t}{\mu}}. \tag{44}$$

We take the following set of parameters as an example for a rough estimation:

$$K = 10^{-17}\ \mathrm{m}^2,\ \mu = 10^{-3}\ \mathrm{Pa{\cdot}s},\ K_\mathrm{f} = 2.2 \times 10^9\ \mathrm{Pa},$$
$$n = 0.22,\ A = 1\ \mathrm{m}^2,\ L = 1\ \mathrm{m},\ \Delta P = 5 \times 10^7\ \mathrm{Pa}.$$

The critical time step is given by Eq. (38):

$$\Delta t_\mathrm{crit} = \frac{10^{-3} \times 0.22 \times 1^2}{2 \times 10^{-17} \times 2.2 \times 10^9}\ \mathrm{s} = 5000\ \mathrm{s}.$$

For several admissible $\Delta t < \Delta t_\mathrm{crit}$, we calculate the seepage velocities of the CSF and LE models based on Eqs. (39) and (42), respectively. The comparison between the seepage velocities is illustrated in Fig. 5. As can be seen that $v_\mathrm{LE} > v_\mathrm{CSF}$ for all admissible Δt. After the same flow duration Δt, the fluid flux is also $Q_\mathrm{LE} > Q_\mathrm{CSF}$. Now, we present the case $\Delta t = 1$ s to show how to compute the seepage velocities and fluid fluxes of the two models.

Based on the CSF model, the seepage velocity (39) and fluid flux (40) are, respectively

$$v_\mathrm{CSF} = \frac{10^{-17}}{10^{-3}} \times \frac{5 \times 10^7}{1/2}\ \mathrm{m/s} = 10^{-6}\ \mathrm{m/s},$$

$Q_{\mathrm{CSF}} = 1 \times 10^{-6} \times 1\ \mathrm{m}^3 = 10^{-6}\ \mathrm{m}^3.$

Based on the proposed LE model, the seepage velocity (42) and fluid flux (44) are, respectively

$$v_{\mathrm{LE}} = \sqrt{\frac{2 \times 10^{-17}}{10^{-3}} \times \frac{5 \times 10^7}{1}}\ \mathrm{m/s} = 10^{-3}\ \mathrm{m/s},$$

$$Q_{\mathrm{LE}} = 1 \times \sqrt{\frac{2 \times 10^{-17} \times (5 \times 10^7) \times 1}{10^{-3}}}\ \mathrm{m}^3 = 10^{-3}\ \mathrm{m}^3.$$

From Fig. 5 and the above calculated results, it can be seen that the seepage velocities and fluid fluxes calculated by the two models differ greatly. The seepage velocity and fluid flux calculated by the LE model can be several orders of magnitude larger than that calculated by the CSF model for admissible flow duration $\Delta t < \Delta t_{\mathrm{crit}}$.

5.2 Estimation schemes

Based on the estimation equations for seepage front in Sect. 5.1, two estimation schemes are proposed. One scheme is the proposed LE model with local mesh refinement, termed the LER estimation method. The other scheme is the proposed LE model with seepage front movement, termed the LEM estimation method.

5.2.1 LER estimation scheme

The first seepage front estimation scheme is the LER model. In this model, the element with an initial element size of L is locally refined along the fluid flow direction, as shown in Fig. 6. After mesh refinement, the element has a smaller size of Δx. The local refinement virtually divides the single element into N small elements:

$$N = \left[\frac{L}{\Delta x}\right], \tag{45}$$

where Δx is also the initial seepage front, which can be estimated by Eq. (43).

The pressure gradients are calculated on the locally refined element, so the accuracy of the pressure gradients can be much enhanced. This will calculate more accurate velocities and fluxes for the seepage flow system. It is also worth mentioning that the local refinement is performed based on the location of seepage front, which makes physical sense.

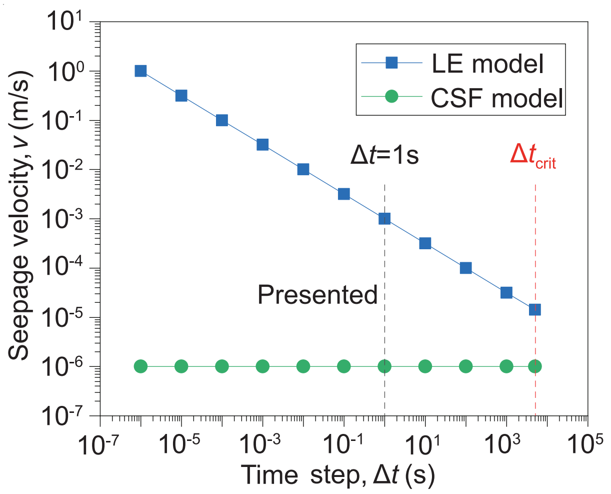

Figure 5 Flow velocity comparison between the LE model and the CSF model.

5.2.2 LEM estimation scheme

The second seepage front estimation scheme is the LEM method. In this model, the seepage front is tracked and moved along the fluid flow direction, as shown in Fig. 7. The seepage front Δx is estimated by Eq. (43) and updated by the following equation at the end of each time step:

$$\Delta x^{t+\Delta t} = \Delta x^{t} + v^{t}\Delta t, \tag{46}$$

where Δx^t and $\Delta x^{t+\Delta t}$ are the estimated seepage front locations at time t and $t + \Delta t$, respectively; v^t is the velocity of seepage front at time t; Δt is the time step.

The pressure gradients are calculated from the latest seepage front, which ensures the accuracy of the pressure gradients. Similar to the LER model, accurate velocities and fluxes can be obtained by the LEM model as well.

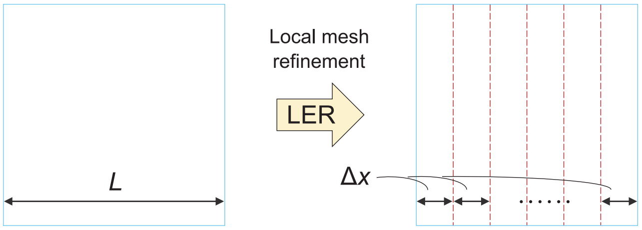

Figure 6 The first seepage front estimation scheme—LER method by local mesh refinement.

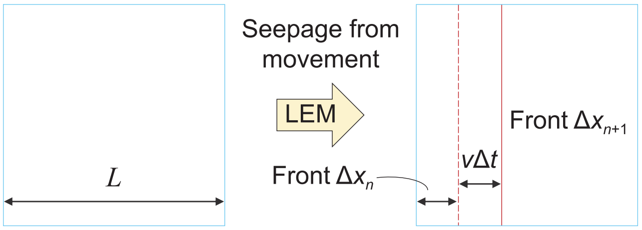

Figure 7 The second seepage front estimation scheme—LEM method by seepage front movement.

Remark 2. The local mesh refinement and the seepage front movement schemes can help capture the details of the seepage flow. Therefore, the proposed LE model can calculate more accurate pressure gradients and hence gives a more accurate flux approximation.

5.3 Implementation procedures

Based on the key equations (42), (43), (31), (35), (27) and (45) or (46), we present the implementation procedures of the CCFVM for the proposed LE seepage flow model:

(1) Initialize the LE pressure field (P^t) by the given initial conditions: $P(\mathbf{x}, t = 0\ \text{s}) = P_0(\mathbf{x})$.

(2) Compute the initial LE seepage velocity ($\mathbf{V}^t$) by Eq. (42) and its increment ($\Delta\mathbf{V}^t$).

(3) Estimate the initial LE seepage front ($\mathbf{x}^t$) based on Eq. (43).

(4) Calculate the LE seepage velocity gradient field ($\nabla\cdot\mathbf{V}^t$) according to Eq. (31).

(5) Calculate the LE pressure field at next time step ($P^{t+\Delta t}$) according to Eq. (35).

(6) Calculate the LE seepage velocity field at next time step ($\mathbf{V}^{t+\Delta t}$) based on Eq. (27).

(7) Alter the mesh information ($\mathbf{x}^{t+\Delta t}$) by Eq. (45) (LER scheme), or update the LE seepage front ($\Delta\mathbf{x}^{t+\Delta t}$) by Eq. (46) (LEM scheme).

(8) Return to Step 3 and advance the time step ($t + \Delta t$).

6. Numerical example with the LER scheme

6.1 Problem description

The numerical model used for the validation of the LER scheme for seepage flow analysis is illustrated in Fig. 8. The model, which has a dimension of 5 m × 2 m × 2 m, is fixed at $z = 5$ m with an inlet pressure boundary $P_{\text{in}} = 50$ MPa and fixed at $z = 0$ m with an outlet pressure boundary $P_{\text{out}} = 0$ MPa, respectively. The parameters used for the numerical simulation are tabulated in Table 1. The simulation time is set to 1 h with an appropriate time step $\Delta t = 1$ s and thus the total number of time steps is 3600.

Table 1 Material parameters used in the numerical simulation

Medium	Parameter	Symbol	Value
Shale	Permeability	K (mD)	0.01
	Porosity	n	0.05
Water	Bulk modulus	K_{f} (GPa)	1.0
	Dynamic viscosity	μ (mPa·s)	1.0
	Density	ρ (kg/m^3)	1000

6.2 Simulation results

The numerical simulations are conducted with two different models—one is the proposed LER model; the other is the conventional seepage flow (CSF) model. The pressure contours at $t = 1$ h using these two different models are shown in Fig. 9. The figure shows that the results obtained from the two models are quite different from each other, which indicates that the proposed model must have considered some extra effects that have a significant influence on the transient seepage process. On the one hand, the LER model gives more accurate estimation of pressure gradients through local mesh refinement. Hence, the model helps capture more details of the seepage flow in a local manner. On the other hand, the local seepage front estimation could calculate large seepage velocity, which may cause significant inertia effect. The LE model considers such effect by introducing an inertia term. The above two effects make the LE seepage model distinguished from the conventional one. Considering these effects makes the new model more physically sound than the conventional one.

Then we plot the seepage flow rates $q = \int v\, dA$ obtained from the two models in Fig. 10. We learn from the figure that the flow rate calculated by the LER model is much higher than that by the CSF model at the initial time. The flow rate by the LER model decreases rapidly after less than $t = 100$ s. After about $t = 500$ s the flow rate obtained from the LER model nearly coincides with that from the CSF model.

Further we integrate the flow rates q over time domain

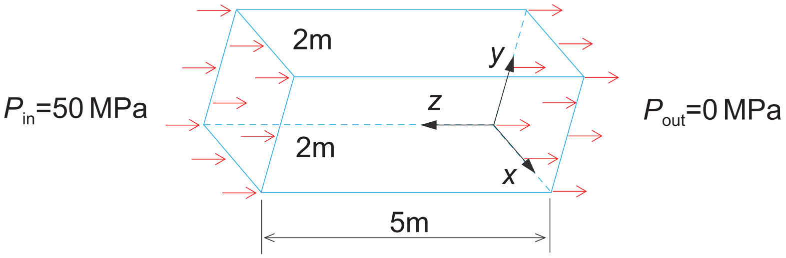

Figure 8 Model setup for the validation of the LER scheme.

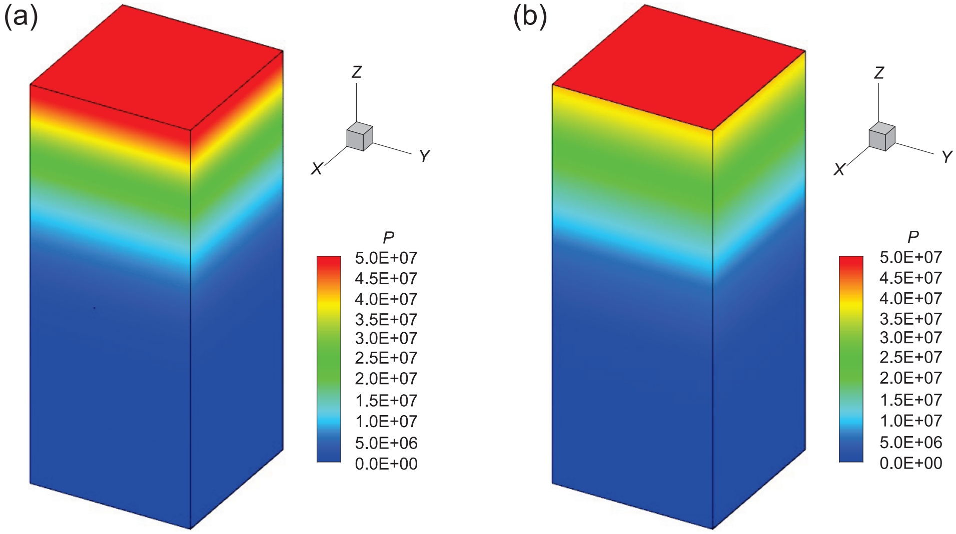

Figure 9 Pressure (unit: Pa) contours at t = 1 h using two different models: **(a)** LER; **(b)** CSF.

and obtain the flow fluxes $Q = \int q\,\mathrm{d}t$ as shown in Fig. 11. The figure shows that the flux calculated by the LER model is higher than that by the CSF model. In the figure, DIFF = LER − CSF, means the flux difference between the LER model and the CSF model. DIFF increases at first and decreases slowly afterwards and it achieves a maximum value of 3.2 L at about t = 600 s. The specific DIFF per unit seepage area is 0.80 L/m^2, which means that the leak-off obtained from the LER model is larger than that from the CSF model. The difference of infiltration thicknesses between the two models is 0.80 mm and it cannot be ignored. The estimation for seepage front by the LE model is of critical importance, which leads to larger pressure gradient and thus larger flow rate and leak-off. In contrast, the traditional seepage flow model obtains smaller pressure gradient and thus smaller flow rate and smaller leak-off.

The pressures at the point (1 m, 1 m, 4 m) obtained from the two models are monitored and illustrated in Fig. 12. The figure shows that the pressures obtained from the two seepage flow models undergo different processes. The pressure obtained from the LER model is smaller at first than that from the CSF model. Then the pressures from the two models meet at a certain point of about t = 1100 s. After that point, the pressure from the LER model exceeds that from the CSF model. The rates of pressure over time are also different between the two models. The LER model gives a smaller rate at first and then a larger one. The rates from the two models tend to be the same at the end of the simulation.

The steady-state pressures obtained from the two models are shown in Fig. 13. The pressures are located at (1 m, 1 m, z), where z ranges from 0 m to 5 m. We learn from the figure that the steady-state pressures using the two models agree well with each other. The apparent reason is that

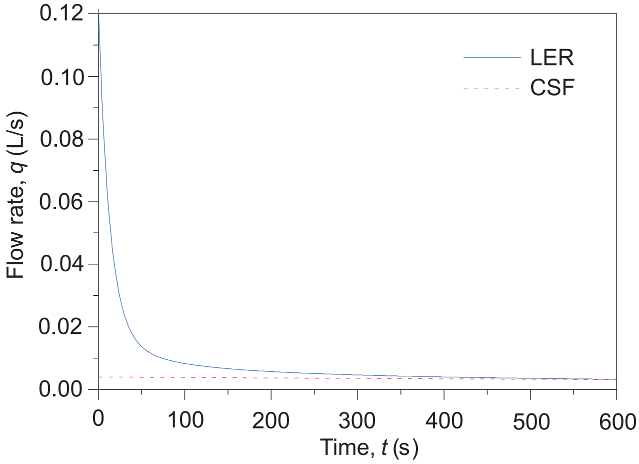

Figure 10 Comparison on flow rate between the LER and CSF models.

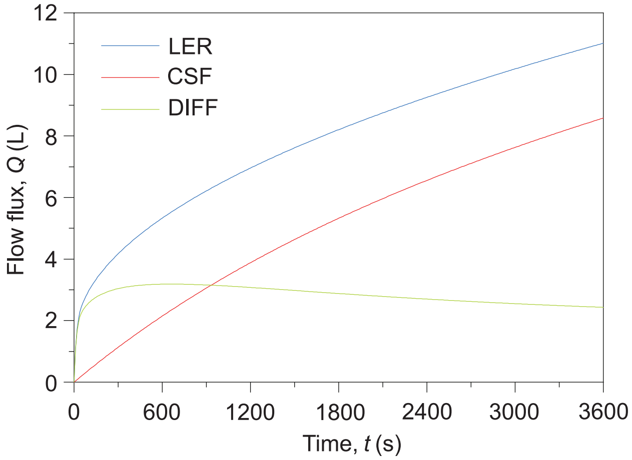

Figure 11 Comparison on flow flux between the LER and CSF models. DIFF = LER − CSF.

the inertia term tends to be 0 when the pressure field slowly

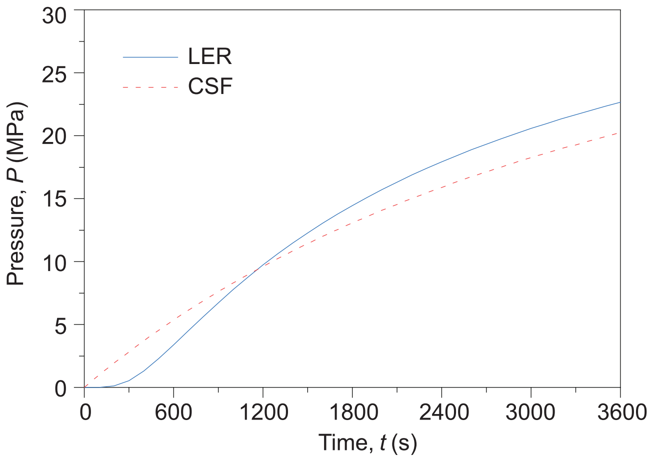

Figure 12 Comparison on pressure at the point (1 m, 1 m, 4 m) between the LER and CSF models.

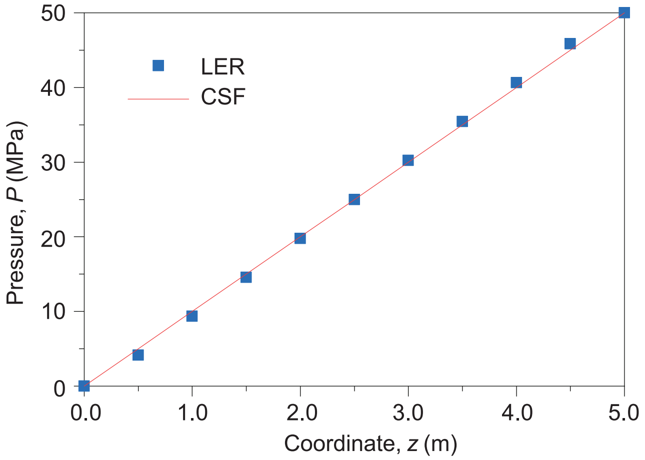

Figure 13 Comparison on steady-state pressure between the LER and CSF models.

gets steady. In this case, the LER model degenerates into the CSF model.

7. Numerical example with the LEM scheme

7.1 Problem description

The numerical model used for the validation of the LEM scheme for seepage flow analysis is illustrated in Fig. 14. The model, which is a cube with size $a = 1$ m, is fixed at $z = 1$ m with an inlet pressure boundary $P_{\mathrm{in}} = 50$ MPa, and fixed at $z = 0$ m with an outlet pressure boundary $P_{\mathrm{out}} = 0$ MPa, respectively. The parameters used for this numerical investigation are the same as that in Sect. 6.1, which are shown in Table 1. The simulation time is set to 100 h with a time step of $\Delta t = 0.1$ s and thus the total number of time steps is 3600000.

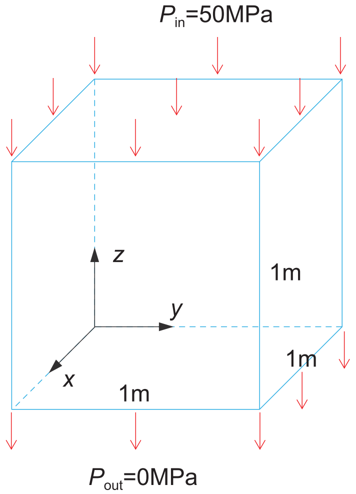

Figure 14 Model setup for the validation of the LEM scheme.

7.2 Simulation results

In the LEM model, the seepage front moves with time, which is highly demonstrated in Fig. 15. The initial seepage front is set to $z = 0.99$ m, which nearly coincides with the top side of the cube. When fluid flows from the top side to the bottom side, the seepage front descends slowly. This phenomenon is well captured by the proposed LEM model. The advantage of the proposed Lagrangian-Eulerian model is that it gives a more physically sound flow process. We also plot the curve of seepage front coordinate versus time in Fig. 16. The figure shows that the seepage front almost descends linearly, which indicates the capability of the presented Lagrangian-Eulerian model for seepage flow analysis.

The flow rates $q = \int v \, dA$ obtained from the LEM and CSF models are compared in Fig. 17. The figure shows that the flow rate calculated by the LEM model is much higher than that by the CSF model near $t = 0$ s. Then the flow rate by the LER model decreases rapidly. After less than $t = 50$ s, the flow rates by the two models nearly coincide with each other. The proposed LEM model well captures the initial large flow rate, which is not observed in the CSF model. When the seepage time is long enough, the two models generate almost the same flow rates.

Further we integrate the flow rates q over time domain and obtain the fluxes $Q = \int q \, dt$ as shown in Fig. 18. The figure indicates that the flux obtained from the LEM model is higher than that from the CSF model. In the figure, DIFF = LEM − CSF, means the flux difference between the LEM and CSF models. DIFF increases at first and decreases slowly afterwards and it achieves a maximum value of 0.23 L at about $t = 40$ s. The difference of infiltration thicknesses between the two models is 0.23 mm and it cannot be ignored. Compared with the LER estimation scheme, the LEM esti-

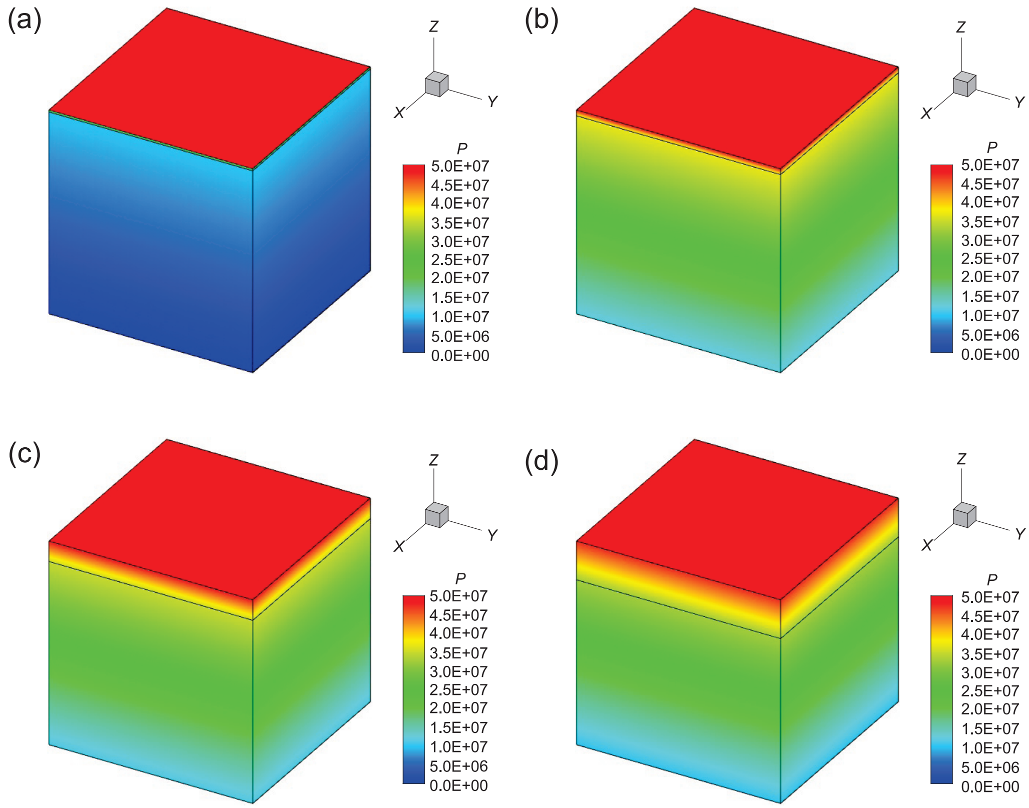

Figure 15 Pressure (unit: Pa) contours considering seepage front movement with the LEM model at different time: **(a)** t = 0 h; **(b)** t = 10 h; **(c)** t = 50 h; **(d)** t = 100 h.

mation scheme is straightforward to implement and efficient to use. The LEM estimation scheme is of critical importance to calculate real leak-off. The proposed Lagrangian-Eulerian model considers a large pressure gradient near the fracture wall while the traditional seepage flow model does not.

7.3 Evaluation of scale effects

The LEM model employs a seepage front movement scheme, which makes the model insensitive to mesh size. In contrast, the CSF model has strong dependence on mesh size. In order to demonstrate the scale effects of both the LEM and CSF models, we focus on the influence of time step Δt in the LEM model and the influence of mesh size Δh in the CSF model. The parameters are shown in Table 2, with four cases considered—two LEM cases and two CSF cases. In the LEM cases (LEM_0.10 and LEM_0.05), a constant mesh size of Δh = 1.00 m is assumed, whereas a constant time step of Δt = 0.10 s is used in the CSF cases (CSF_1.00 and CSF_0.50).

Table 2 Numerical cases for the evaluation of scale effects

Scale	Model	Symbol	Value	Case
Time	LEM	Δt (s)	0.10	LEM_0.10
			0.05	LEM_0.05
Space	CSF	Δh (m)	1.00	CSF_1.00
			0.50	CSF_0.50

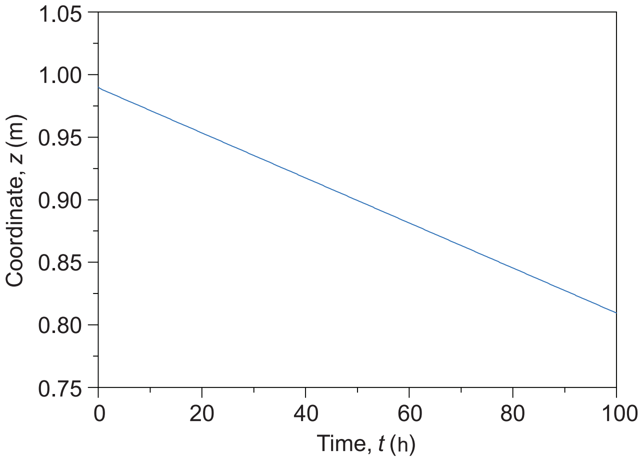

Figure 16 Seepage front movement: coordinate z versus time t.

The flow rates in four different cases are compared in Fig. 19. The figure shows that the flow rates in both LEM cases are larger than those in both CSF cases at initial time. Afterwards, all the flow rates tend to be close to each other, except the flow rate in case CSF_0.50, which is a little larger. This is because the three cases use the same mesh size Δh = 1.00 m

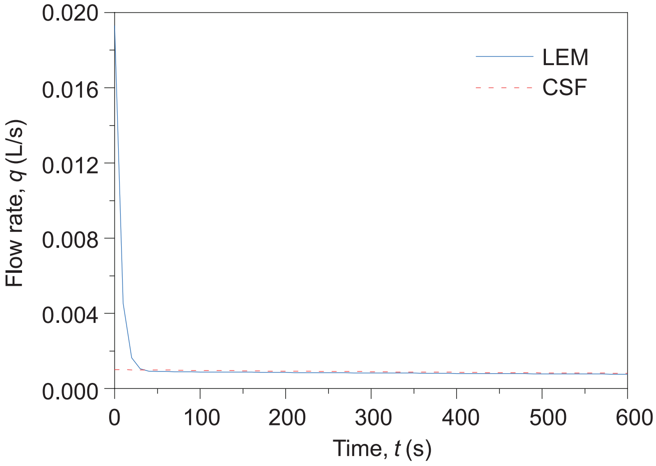

Figure 17 Comparison on flow rate between the LEM and CSF models.

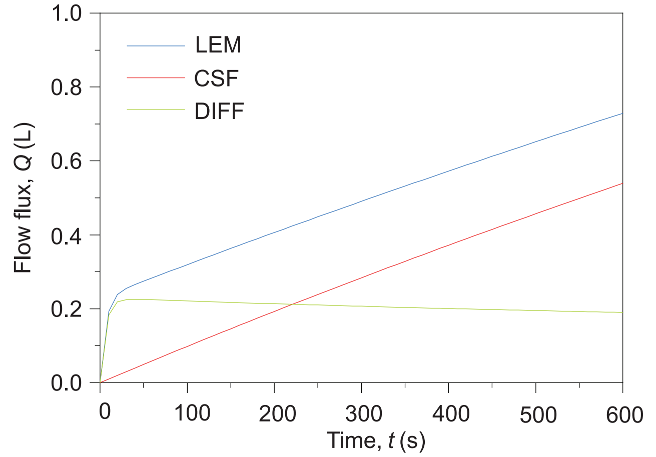

Figure 18 Comparison on flow flux between the LEM and CSF models. DIFF = LEM – CSF.

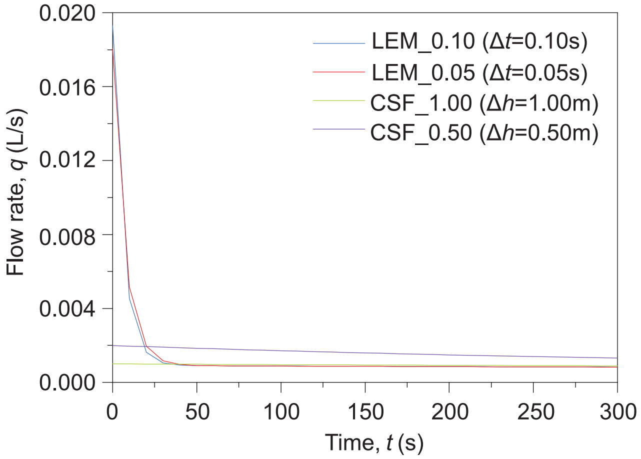

Figure 19 Comparison on flow rate among the four cases with the LEM and CSF models.

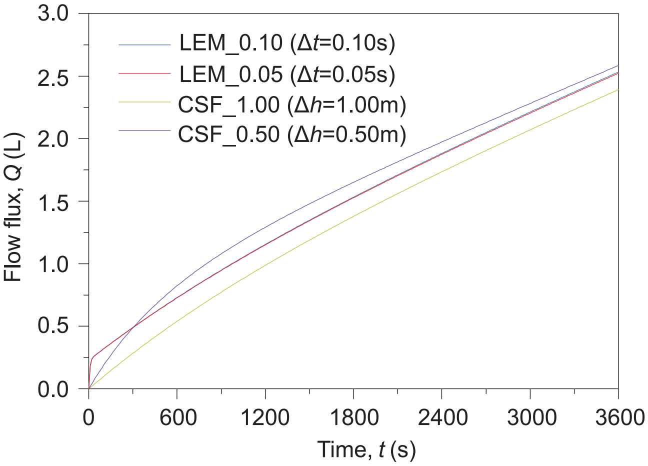

Figure 20 Comparison on flow flux among the four cases with the LEM and CSF models.

other than the case CSF_0.50 uses a smaller mesh size $\Delta h = 0.50$ m. The flow rates in the LEM cases are very close to each other, but that is not true for the CSF cases. The flow rate in CSF_0.50 can be twice as much as that in CSF_1.00. This means that the LEM model has little scale effect (no dependency on temporal scale) while the CSF model has much scale effect (dependency on spatial scale).

The flow fluxes in all the four cases, which are integrated from the flow rates over time domain, are compared in Fig. 20. The figure indicates that the LEM model has almost no dependency on time step but the CSF model has strong dependency on mesh size. The fluxes in LEM cases keep in good consistency with each other, but it is not true for the fluxes in CSF cases. We also know from the figure that the fluxes in four different cases are close to each other when seepage time is long enough. The fluxes in both models tend to agree well with each other, when fluid flow in the porous medium gets steady.

7.4 Comparison between LEM and LER schemes

We use the same numerical model, as presented in Sect. 7.1, to compare the proposed two LE schemes. The seepage flow rates obtained from the LEM and LER schemes are depicted in Fig. 21, which shows some similarities between the two schemes. At initial time, both the two schemes give very large flow rates. Afterwards, the flow rates drop down soon till about $t = 40$ s. After $t = 450$ s, the two schemes present almost the same flow rates, which indicates the consistency of the two schemes. The difference between the two schemes lies in the rate of change in the seepage flow rate at the time interval $20\text{ s} \le t \le 200\text{ s}$. Since different seepage front estimation schemes are used, this difference is quite reasonable.

The flow fluxes by the two schemes are integrated from the flow rates in the temporal domain. A detailed comparison between the two schemes on flow flux is presented in Fig. 22. The two schemes share similar trends in the increase of flow

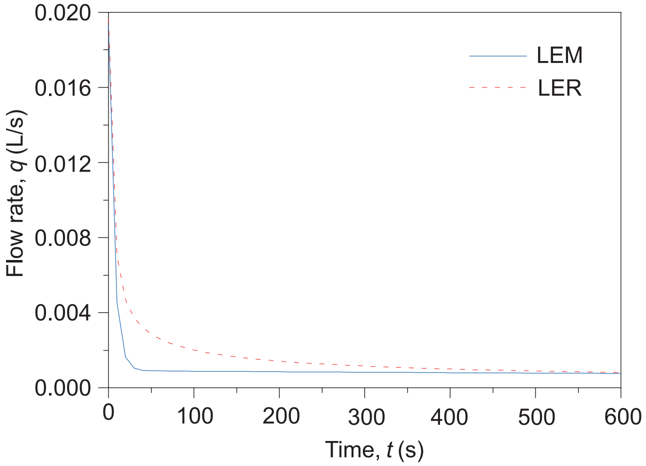

Figure 21 Comparison on flow rate between the LEM and LER models.

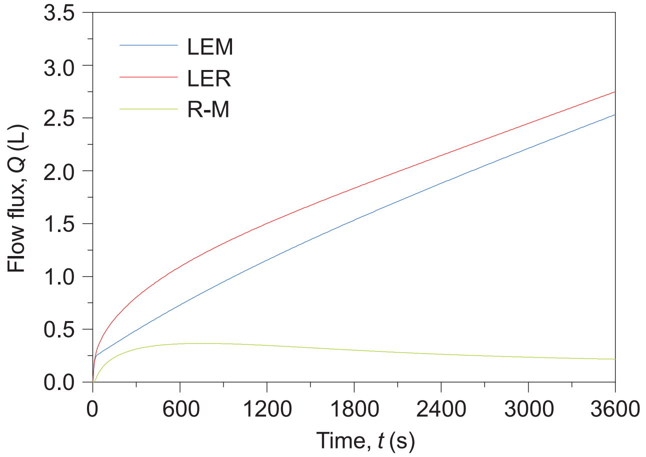

Figure 22 Comparison on flow flux between the LEM and LER models. "R-M" denotes the flux difference between the LER and LEM models.

flux. The different flow rates, though little, produce a narrow gap between the flow fluxes of the two LE schemes.

8. Conclusions

Most conventional numerical models employ PDEs to describe a seepage flow system and use weighted residual and finite difference solution techniques to solve the PDEs. These PDEs are established in view of a spatial point, which mathematically stems from the infinitesimal concept. We develop an alternative approach based on the energy approach, i.e., the Lagrange's equations, to the representation of the seepage flow system.

The Lagrange's functional (Lagrangian) is established on an RVE by integrating the energy on the RVE. Following a Lagrange equation formulation, the variation of the Lagrangian results in a set of integral equations, which are described in a mixed Lagrangian-Eulerian frame (LE model). The equations are numerically discretized with a cell-centered FVM. Two seepage front estimation schemes—the LER and LEM schemes, are introduced. The resulting model is a true energy formulation, developed without reference to the partial differential momentum equations. Two examples using the LER and LEM schemes are demonstrated to validate the proposed LE model.

The example using LER seepage front estimation scheme shows that:

(1) The flow rate using LER is high at initial time and decreases rapidly. At last the flow rate using LER is close to that using CSF.

(2) Integrated from flow rate over time domain, the flux using LER is much larger than that using CSF. The flux difference between the two models cannot be ignored (the maximum difference can reach 0.80 L per unit seepage area).

(3) The results using both models are close when seepage time is long enough. The steady-state pressure fields using both models agree well with each other.

The example with LEM seepage front estimation scheme shows that:

(1) The flow rate using LEM is high at initial time and it decreases rapidly. At last the flow rate using LEM is close to that using CSF.

(2) Integrated from flow rate over time domain, the flux using LEM is larger than that using CSF. The flux difference between the two models cannot be ignored (the maximum difference can reach 0.23 L per unit seepage area).

(3) The proposed model with LEM seepage front estimation has almost no scale effect, whereas the CSF model is quite dependent on the mesh size scale. Besides, the leak-off using LEM is close to that using CSF when seepage time is long enough. Therefore, both models present the same steady state of seepage flow.

The comparison between the LEM and LER schemes indicates that:

(1) The comparison on flow rates shows some similarities between the two LE schemes. The flow rates are large at initial time, drop down soon and tends to be a stable value after a long period.

(2) The difference of flow rates by the two schemes, though little, produces a narrow gap between the flow fluxes of the two schemes.

In hydraulic fracturing, the fracture area can be very huge, and thus the leak-off simulated from the proposed Lagrangian-Eulerian model can be much larger than the CSF model. The LE results are more physically sound according to the monitored leak-off data. Therefore, the proposed LE model (LER and LEM) is more capable of dealing with leak-off problems in hydraulic fracturing. Besides, the model has no dependency on spatial scale, which shows its tremendous advantages.

On-going work is to couple the proposed seepage flow model with the stress field modeled by continuous-discontinuous element method (CDEM) [50-52] for a wider range of geotechnical applications, such as hydraulic fracturing simulation [53-55]. The proposed LE seepage flow model can also be combined with other novel numerical models, such as numerical manifold method (NMM) [56-58], extended finite element method (XFEM) [59-62], cracking elements method [63-65], peridynamics model (PD) [66,67], and scaled-boundary finite element method (SBFEM) [68].

Appendix A. Abbreviations

The following abbreviations are used in this paper:

PDE	Partial differential equation
RVE	Representative volume element
FEM	Finite element method
FDM	Finite difference method
FVM	Finite volume method
NMM	Numerical manifold method
VEM	Virtual element method
XFEM	eXtended FEM
PD	Peridynamics model
SBFEM	Scaled-boundary FEM
CCFVM	Cell-centered FVM
CSF	Conventional seepage flow model
LHS	Left-hand side
RHS	Right-hand side
LE	Lagrangian-Eulerian model
LER	LE with local mesh refinement
LEM	LE with seepage front movement
DIFF	flux difference between two models

Appendix B. Seepage flow parameter systems

Different parameter systems of seepage flow are used in different fields. For example, in hydraulic engineering, hydraulic conductivity is preferred as the measure of how well a porous medium allows water to flow through it. However, in petroleum engineering, permeability is used as the measure of the ease with which a fluid can move through a porous medium. In order to understand the parameter systems of seepage flow in different fields, we tabulate them in Table B1.

Appendix C. Formulation of CCFVM

We neglect the body force for simplicity during the formulation. The Darcy's velocity term in Eq. (27) can be written as

$$\mathbf{v}_{\mathrm{D}} = -\frac{k}{\rho g}\nabla p = -\frac{K}{\mu}\nabla p = -\kappa\nabla p. \tag{C1}$$

Now we formulate the cell-centered FVM [43, 44]. The flow velocities along line segments C_iC_o and C_oC_j can be respectively written as

$$\mathbf{v}_{io} = -\kappa_i\nabla p_{io} = -\kappa_i\frac{p_o - p_i}{D_i}(-\mathbf{d}_i), \tag{C2}$$

$$\mathbf{v}_{oj} = -\kappa_j\nabla p_{oj} = -\kappa_j\frac{p_j - p_o}{D_j}\mathbf{d}_j. \tag{C3}$$

The flux rate across the interface $\partial\Omega_{ij}$ can be computed from the following integral:

$$q_{ij} = q_{io} = \int_{\partial\Omega_{ij}} \mathbf{v}_{io}\cdot(-\mathbf{n}_i)\,\mathrm{d}S = A\kappa_i\frac{p_i - p_o}{D_i}(\mathbf{d}_i\cdot\mathbf{n}_i), \tag{C4}$$

$$q_{ij} = q_{oj} = \int_{\partial\Omega_{ij}} \mathbf{v}_{oj}\cdot\mathbf{n}_j\,\mathrm{d}S = A\kappa_j\frac{p_o - p_j}{D_j}(\mathbf{d}_j\cdot\mathbf{n}_j), \tag{C5}$$

where A is the area of the interface between the two adjacent cells, κ_i is the permeability coefficient of cell Ω_i, D_i is the distance between the cell center and the interface center, $\mathbf{n}_i$ is the unit vector normal to the interface and $\mathbf{d}_i$ is the unit vector along C_oC_i. Detailed definitions of these symbols are shown in Fig. C1.

We can get (p_ip_o) and (p_op_j) from Eqs. (C4) and (C5), respectively. Adding the two terms gives

$$p_i - p_j = \left[\frac{D_i}{A\kappa_i(\mathbf{d}_i\cdot\mathbf{n}_i)} + \frac{D_j}{A\kappa_j(\mathbf{d}_j\cdot\mathbf{n}_j)}\right]q_{ij}. \tag{C6}$$

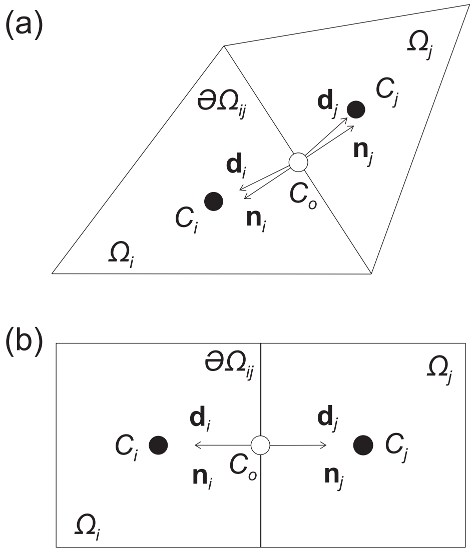

Figure C1 Geometry representation of two adjacent cells (Ω_i and Ω_j) in two dimensions: **(a)** unstructured mesh; **(b)** structured mesh. The solid dot indicates the cell center and the hollow dot indicates the interface center.

Table B1 Comparison among different parameter systems of seepage flow

Field	Hydraulics			Petroleum		Geomechanics
Terminology	Hydraulic conductivity	Density	Gravity	Permeability	Dynamic viscosity	Permeability coefficient
Symbol	k	ρ_f	g	K	μ	κ
Dimension	$[\mathrm{LT}^{-1}]$	$[\mathrm{ML}^{-3}]$	$[\mathrm{LT}^{-2}]$	$[\mathrm{L}^2]$	$[\mathrm{ML}^{-1}\mathrm{T}^{-1}]$	$[\mathrm{M}^{-1}\mathrm{L}^3\mathrm{T}]$
SI unit	m/s	kg/m^3	m/s^2	m^2	Pa·s	m^2/(Pa·s)
Conversion	$k/(\rho_\mathrm{f} g) = K/\mu = \kappa$					

By denoting

$$\alpha_i = \frac{A\kappa_i}{D_i}(\mathbf{d}_i \cdot \mathbf{n}_i), \quad \alpha_j = \frac{A\kappa_j}{D_j}(\mathbf{d}_j \cdot \mathbf{n}_j) \tag{C7}$$

and

$$T_{ij} = \frac{\alpha_i \alpha_j}{\alpha_i + \alpha_j}, \tag{C8}$$

Eq. (C6) can be simplified as

$$q_{ij} = T_{ij}(p_i - p_j), \tag{C9}$$

where T_{ij} represents the transmissibility between cell Ω_i and cell Ω_j.

Summing up all the flux rates from adjacent cells (Ω_j) by Eq. (C9) at time t, we can formulate Eq. (32) as follows:

$$q_{i,1}^t = \sum\nolimits_j q_{ij}^t = \sum\nolimits_j T_{ij}(p_i^t - p_j^t). \tag{C10}$$

Conflict of interest *On behalf of all authors, the corresponding author states that there is no conflict of interest.*

Author contributions ***Li-Xiang Wang:*** *Conceptualization, Methodology, Software, Validation, Formal analysis, Investigation, Data curation, Writing – original draft preparation, Writing – review and editing, Visualization, Funding acquisition.* ***Shi-Hai Li:*** *Conceptualization, Methodology, Formal analysis, Investigation, Resources, Writing – review and editing, Supervision, Project administration, Funding acquisition.* ***Chun Feng:*** *Conceptualization, Methodology, Formal analysis, Investigation, Resources, Writing – review and editing, Supervision, Project administration, Funding acquisition.*

Acknowledgements *This work was supported by the National Natural Science Foundation of China (Grant No. 12102059), and the National Key Research and Development Program of China (Grant No. 2018YFC1505504).*

1 H. Darcy, Les Fontaines Publiques de la Ville de Dijon (Dalmon, Paris, 1856).

2 S. Whitaker, Flow in porous media I: A theoretical derivation of Darcy's law, Transp. Porous. Media **1**, 3 (1986).

3 W. W. Woessner, and E. P. Poeter, Hydrogeologic Properties of Earth Materials and Principles of Groundwater Flow (The Groundwater Project, Guelph, 2020).

4 R. Wheaton, Chapter 5 - Numerical simulation methods for predicting reservoir performance, in: Fundamentals of Applied Reservoir Engineering (Gulf Professional Publishing, 2016), pp. 107-125.

5 C. Zhang, J. Chai, J. Cao, Z. Xu, Y. Qin, and Z. Lv, Numerical simulation of seepage and stability of tailings dams: A case study in Lixi, China, Water **12**, 742 (2020).

6 K. Ma, C. A. Tang, L. X. Wang, D. H. Tang, D. Y. Zhuang, Q. B. Zhang, and J. Zhao, Stability analysis of underground oil storage caverns by an integrated numerical and microseismic monitoring approach, Tunnelling Underground Space Tech. **54**, 81 (2016).

7 A. Aharmouch, B. Amaziane, M. El Ossmani, and K. Talali, A fully implicit finite volume scheme for a seawater intrusion problem in coastal aquifers, Water **12**, 1639 (2020).

8 S. Yu, One-dimensional flow model for coal-gas outbursts and initiation criterion, Acta Mech. Sin. **8**, 363 (1992).

9 A. Younes, M. Fahs, and P. Ackerer, Modeling of Flow and transport in saturated and unsaturated porous media, Water **13**, 1088 (2021).

10 S. Majid Hassanizadeh, and A. Leijnse, A non-linear theory of high-concentration-gradient dispersion in porous media, Adv. Water Resour. **18**, 203 (1995).

11 S. Liu, and J. H. Masliyah, Non-linear flows in porous media, J. Non-Newtonian Fluid Mech. **86**, 229 (1999).

12 G. Q. Zhou, Y. Zhou, and X. Y. Shi, One-dimensional non-Darcy flow in a semi-infinite porous media: A multiphase implicit Stefan problem with phases divided by hydraulic gradients, Acta Mech. Sin. **33**, 855 (2017).

13 G. Tao, Z. Huang, H. Xiao, W. Zhao, and Q. Luo, A new nonlinear seepage model for clay soil considering the initial hydraulic gradient of microscopic seepage channels, Comput. Geotech. **154**, 105179 (2023).

14 R.-Z. Yu, Q. Lei, Z.-M. Yang, and Y.-N. Bian, Nonlinear flow numerical simulation of an ultra-low permeability reservoir, Chin. Phys. Lett. **27**, 074702 (2010).

15 Y.-S. Wu, Non-Darcy Flow of Immiscible Fluids. In: Multiphase Fluid Flow in Porous and Fractured Reservoirs (Elsevier, 2016), pp. 167-206.

16 O. Zienkiewicz, P. Mayer, and Y. K. Cheung, Solution of Anisotropic seepage by finite elements, J. Eng. Mech. Div. **92**, 111 (1966).

17 R. W. Jeppson, Finite Difference Solutions to Free-Surface Flow Through Nonhomogeneous Porous Media (Report of Utah State University, Logan, 1967), p. 316.

18 S. P. Neuman, and P. A. Witherspoon, Finite element method of analyzing steady seepage with a free surface, Water Resour. Res. **6**, 889 (1970).

19 S. P. Neuman, Saturated-unsaturated seepage by finite elements, J. Hydr. Div. **99**, 2233 (1973).

20 B. Das, S. Steinberg, S. Weber, and S. Schaffer, Finite difference methods for modeling porous media flows, Transp. Porous. Media **17**, 171 (1994).

21 H. Zheng, D. F. Liu, C. F. Lee, and L. G. Tham, A new formulation of Signorini's type for seepage problems with free surfaces, Int. J. Numer. Meth. Eng. **64**, 1 (2005).

22 C. Chávez-Negrete, F. J. Domínguez-Mota, and D. Santana-Quinteros, Numerical solution of Richards' equation of water flow by generalized

finite differences, Comput. Geotech. **101**, 168 (2018).

23 V. Sharma, K. Fujisawa, and A. Murakami, Space-time finite element method for transient and unconfined seepage flow analysis, Finite Elem. Anal. Des. **197**, 103632 (2021).

24 M. Karimi-Fard, L. J. Durlofsky, and K. Aziz, An efficient discrete-fracture model applicable for general-purpose reservoir simulators, SPE J. **9**, 227 (2004).

25 E. Bresciani, P. Davy, and J. R. de Dreuzy, A finite volume approach with local adaptation scheme for the simulation of free surface flow in porous media, Int. J. Numer. Anal. Meth. Geomech. **36**, 1574 (2012).

26 I. Stefansson, I. Berre, and E. Keilegavlen, Finite-volume discretisations for flow in fractured porous media, Transp. Porous. Media **124**, 439 (2018).

27 H. Zheng, F. Liu, and C. Li, Primal mixed solution to unconfined seepage flow in porous media with numerical manifold method, Appl. Math. Model. **39**, 794 (2015).

28 M. Hu, J. Rutqvist, and Y. Wang, A practical model for fluid flow in discrete-fracture porous media by using the numerical manifold method, Adv. Water Resour. **97**, 38 (2016).

29 L. Zhou, Y. Wang, and D. Feng, A high-order numerical manifold method for Darcy flow in heterogeneous porous media, Processes **6**, 111 (2018).

30 Y. Chen, H. Zheng, B. Yin, and W. Li, The MLS-based numerical manifold method for Darcy flow in heterogeneous porous media, Eng. Anal. Bound. Elem. **148**, 220 (2023).

31 X. Liu, and Y. P. Xiao, Meshfree numerical solution of two-phase flow through porous media, in: Computational Methods, edited by G. R. Liu, V. B. C. Tan, and X. Han (Springer, Dordrecht, 2006), pp. 1547-1553.

32 R. Campagna, S. Cuomo, S. De Marchi, E. Perracchione, and G. Severino, A stable meshfree PDE solver for source-type flows in porous media, Appl. Numer. Math. **149**, 30 (2020).

33 B. Wang, J. Li, Q. Jiang, Y. Yang, and X. T. Feng, An improved FE-Meshfree method for solving steady seepage problems, Comput. Geotech. **119**, 103223 (2020).

34 M. F. Benedetto, A. Borio, F. Kyburg, J. Mollica, and S. Scialó, An arbitrary order Mixed Virtual Element formulation for coupled multi-dimensional flow problems, Comput. Methods Appl. Mech. Eng. **391**, 114204 (2022).

35 R. Abraham, and J. E. Marsden, Foundations of Mechanics, 2nd ed. (AMS Chelsea Publishing, Rhode Island, 2008), pp. 159-252.

36 J. A. Shapiro, Classical Mechanics, Course for Physics 507 (Rutgers University, Rutgers, 2010), pp. 35-64.

37 E. P. Fahrenthold, and J. C. Koo, Discrete Hamilton's equations for viscous compressible fluid dynamics, Comput. Methods Appl. Mech. Eng. **178**, 1 (1999).

38 J. C. Koo, and E. P. Fahrenthold, Discrete Hamilton's equations for arbitrary Lagrangian-Eulerian dynamics of viscous compressible flow, Comput. Methods Appl. Mech. Eng. **189**, 875 (2000).

39 B. A. Horban, and E. P. Fahrenthold, Hamilton's equations for impact simulations with perforation and fragmentation, J. Dynamic Syst. Measurement Control **127**, 617 (2005).

40 E. P. Fahrenthold, and C. R. Hean, Discrete Lagrange equations for thermofluid systems, J. Dyn. Syst. Meas. Control **130**, 011009 (2008).

41 C. R. Hean, and E. P. Fahrenthold, Discrete Lagrange equations for reacting thermofluid dynamics in arbitrary Lagrangian-Eulerian frames, Comput. Methods Appl. Mech. Eng. **313**, 303 (2017).

42 L. F. Liang, Q. Y. Guo, and H. Y. Song, Analytical dynamics of continuous medium and its application, Adv. Mech. **49**, 201908 (2019).

43 L. X. Wang, S. H. Li, and Z. S. Ma, in A finite volume simulator for single-phase flow in fractured porous media: Proceedings of the Sixth International Conference on Discrete Element Methods and Related Techniques, Colorado School of Mines, Golden, 2013, pp. 130-135.

44 L. Wang, S. Li, Z. Ma, and C. Feng, A cell-centered finite volume method for fluid flow in fractured porous media and its parallelization with OpenMP, Chin. J. Rock Mech. Eng. **34**, 865 (2015).

45 J. Siddique, A. Ahmed, A. Aziz, and C. Khalique, A review of mixture theory for deformable porous media and applications, Appl. Sci. **7**, 917 (2017).

46 S. Bandara, and K. Soga, Coupling of soil deformation and pore fluid flow using material point method, Comput. Geotech. **63**, 199 (2015).

47 K. R. Arora, Soil Mechanics and Foundation Engineering, 7th ed. (Standard Publishers Distributors, Delhi, 2009).

48 J. C. Strikwerda, Finite Difference Schemes and Partial Differential Equations, 2nd ed. (Society for Industrial and Applied Mathematics, 2004), pp. 137-163.

49 G. W. Recktenwald, Finite-Difference Approximations to the Heat Equation (2011), pp. 1-27.

50 S. Li, M. Zhao, Y. Wang, and Y. Rao, A new numerical method for DEM-block and particle model, Int. J. Rock Mech. Min. Sci. **41**, 436 (2004).

51 L. Wang, S. Li, G. Zhang, Z. Ma, and L. Zhang, A GPU-based parallel procedure for nonlinear analysis of complex structures using a coupled FEM/DEM approach, Math. Problems Eng. **2013**, 618980 (2013).

52 C. Feng, X. Liu, Q. Lin, and S. Li, A simple particle-spring method for capturing the continuous-discontinuous processes of brittle materials, Eng. Anal. Bound. Elem. **139**, 221 (2022).

53 L. Wang, D. Tang, S. Li, J. Wang, and C. Feng, Numerical simulation of hydraulic fracturing by a mixed method in two dimensions (in Chinese), Chin. J. Theor. Appl. Mech. **47**, 973 (2015).

54 X. Zhu, C. Feng, P. Cheng, X. Wang, and S. Li, A novel three-dimensional hydraulic fracturing model based on continuum-discontinuum element method, Comput. Methods Appl. Mech. Eng. **383**, 113887 (2021).

55 Q. Ren, Y. Zhao, X. Zhu, Y. Zhou, Y. Jiang, P. Wang, and C. Zhang, CDEM-based simulation of the 3D propagation of hydraulic fractures in heterogeneous Coalbed Methane reservoirs, Comput. Geotech. **152**, 104992 (2022).

56 Y. J. Ning, X. M. An, Q. Lü, and G. W. Ma, Modeling rock failure using the numerical manifold method followed by the discontinuous deformation analysis, Acta Mech. Sin. **28**, 760 (2012).

57 H. Zheng, F. Liu, and X. Du, Complementarity problem arising from static growth of multiple cracks and MLS-based numerical manifold method, Comput. Methods Appl. Mech. Eng. **295**, 150 (2015).

58 Y. Yang, G. Sun, and H. Zheng, A high-order numerical manifold method with continuous stress/strain field, Appl. Math. Model. **78**, 576 (2020).

59 L. X. Wang, L. F. Wen, J. T. Wang, and R. Tian, Implementations of parallel software for crack analyses based on the improved XFEM, Sci. Sin.-Tech. **48**, 1241 (2018).

60 R. Tian, L. Wen, and L. Wang, Three-dimensional improved XFEM (IXFEM) for static crack problems, Comput. Methods Appl. Mech. Eng. **343**, 339 (2019).

61 L. Wang, L. Wen, G. Xiao, and R. Tian, A templated method for partitioning of solid elements in discontinuous problems (in Chinese), Chin. J. Theor. Appl. Mech. **53**, 823 (2021).

62 L. F. Wen, R. Tian, L. X. Wang, and C. Feng, Improved XFEM for multiple crack analysis: Accurate and efficient implementations for stress intensity factors, Comput. Methods Appl. Mech. Eng. **411**, 116045 (2023).

63 Y. Zhang, and H. A. Mang, Global cracking elements: A novel tool for Galerkin-based approaches simulating quasi-brittle fracture, Int. J. Numer. Methods Eng. **121**, 2462 (2020), arXiv: 1908.06268.

64 Y. Zhang, Z. Gao, Y. Li, and X. Zhuang, On the crack opening and energy dissipation in a continuum based disconnected crack model, Finite Elem. Anal. Des. **170**, 103333 (2020).

65 Y. Zhang, J. Huang, Y. Yuan, and H. A. Mang, Cracking elements method with a dissipation-based arc-length approach, Finite Elem. Anal. Des. **195**, 103573 (2021).

66 Y. Zhang, X. Yang, X. Wang, and X. Zhuang, A micropolar peridynamic model with non-uniform horizon for static damage of solids considering different nonlocal enhancements, Theor. Appl. Fract. Mech. **113**, 102930 (2021).

67 S. Yang, X. Gu, Q. Zhang, and X. Xia, Bond-associated non-ordinary state-based peridynamic model for multiple spalling simulation of concrete, Acta Mech. Sin. **37**, 1104 (2021).

68 Z. Yang, Application of scaled boundary finite element method in static and dynamic fracture problems, Acta Mech. Sin. **22**, 243 (2006).

混合拉格朗日-欧拉描述的多孔介质渗流拉格朗日方程

王理想, 李世海, 冯春

摘要 传统数值模型大多使用偏微分方程来描述渗流问题, 并使用加权余量和有限差分技术来求解该方程. 这类方程建立在空间点的角度之上, 在数学上源于无穷小的概念. 本文发展了一种求解渗流问题的能量方法, 将拉格朗日方程应用于渗流系统的描述, 而非直接采用偏微分方程进行描述. 通过对代表性体积单元的能量进行积分而建立拉格朗日泛函, 并采用合理的广义坐标对该泛函进行变分得到系统控制方程. 将所得到的积分方程, 由拉格朗日描述转化为欧拉描述, 以此提高计算精度. 然后, 使用中心型有限体积法对控制方程进行数值离散. 最后, 给出了两种渗流前缘评估方案：一种方案通过网格局部细化实现, 另一种方案利用渗流前缘移动实现. 本文所提出的模型是一个建立在能量观点上的模型, 而非建立在偏微分动量方程基础之上. 数值算例表明, 该模型可给出物理上合理的计算结果.